Fracture behavior in CFRP cross-ply laminates with initially cut fibers

Yashiro, Shigeki
Graduate School of Science and Engineering, Ehime University

Ogi, Keiji
Graduate School of Science and Engineering, Ehime University

https://hdl.handle.net/2324/4476057

出版情報：Composites Part A: Applied Science and Manufacturing. 40 (6-7), pp.938-947, 2009-05-04. Elsevier
バージョン：
権利関係：

Composites: Part A 40 (2009) 938–947
DOI: 10.1016/j.compositesa.2009.04.023

Fracture behavior in CFRP cross-ply laminates with initially cut fibers

S. Yashiro [a,*], K. Ogi [a]

[a] Graduate School of Science and Engineering, Ehime University,

3 Bunkyo-cho, Matsuyama, Ehime 790-8577, Japan

[*] Corresponding author: Tel: +81-89-927-9811; Fax: +81-89-927-9811.

E-mail address: yashiro@eng.ehime-u.ac.jp (S. Yashiro)

Abstract

This study qualitatively investigates the effects of initially cut fibers (slits) on fracture behavior in carbon fiber reinforced plastic (CFRP) cross-ply laminates, which had alternate or identical slit angle $\pm\theta$ in the 0° plies. Damage progress during tensile tests was observed for several geometries of cutting. We also numerically evaluated fracture behavior in laminates with slits by a layer-wise finite-element model with cohesive elements. The simulated damage patterns included matrix cracks along the slits, splits in the 0° layer from the slit tips, and transverse cracks in the 90° layer. Delamination was also generated at the crossing point of ply cracks due to the large shear stress, and then extended to form the triangular region bounded by the slits and splits. The predicted damage extension to the final failure agreed with the observations. A numerical study demonstrated that the damage near the slits produced a stress field similar to that of a penetrating notch.

Keywords: A. Polymer-matrix composites (PMCs); B. Delamination; C. Finite element analysis (FEA); B. Stress concentrations.

1. Introduction

Carbon fiber reinforced plastics (CFRPs) have frequently been applied to various structures because of their light weight, high strength and modulus, and superior fatigue properties. When complex-shaped components are manufactured, they contain discontinuities of reinforcing fibers. For example, fibers in prepreg sheets might be bent and broken at a sharp corner. When a component is manufactured through the resin transfer molding method, the preform is cut before fabrication to achieve the designed geometry. Although sheet molding compounds (SMCs) have good molding ability, their strength is much lower than that of composites with continuous fibers, and they have large variation, due to the many ends of fiber bundles [1-3]. Thus, such composite components may have fiber ends or initially cut fibers that degrade the mechanical properties of CFRP.

Taketa et al. [4,5] recently developed a new sheet molding compound, termed unidirectionally arrayed chopped strand (UACS) by regularly introducing slits into the prepreg sheets. UACS achieved higher strength than conventional SMC materials through control of the fiber direction and the position of fiber ends, as well as the shaping performance of molding sheets.

Initial breakage in continuous fibers induces complicated fracture behavior and serious strength degradation. Many researchers have studied the strength and the damage process in notched composite laminates where all the plies were initially damaged [6-8]. Beaumont and his colleagues [9-12] discussed in detail the notched strength, post-fatigue properties, and the damage state near the notches. They also proposed a simple analytical model for estimating damage growth and strength in notched laminates. Olsson et al. [13] studied strain concentration in quasi-isotropic laminates with holes or with cut fibers, and discussed the degradation of tensile strength due to fiber breakage near the impact point. They provided a closed-form prediction of strain fields, and predicted the softening properties of artificial damage by an inverse method. Craven et al. [14] studied stiffness reductions generated by various crack patterns in the reinforcing fibers in multidirectional laminates. However, the effects of cut fibers on fracture behavior and strength have not been reported, despite their importance.

In the present study, the damage progress from the ends of cut fibers in CFRP laminates was experimentally and numerically investigated. We manufactured cross-ply laminates from CFRP prepreg sheets with initially cut fibers (slits) as a model laminate with fiber ends. Then, the fracture process and the tensile strength of the laminates were experimentally investigated in terms of slit geometries. This study also numerically predicted the damage extension near the slit to qualitatively understand the fracture behavior from the cut fibers, and considered the effects of slits on fracture behavior.

2. Experimental procedure

In order to clarify the mechanism of damage extension from the fiber ends, we used coupon specimens with a simple stacking configuration and a constant slit angle. A cross-ply laminate was manufactured by using CFRP prepreg sheets (T700S/#2521R, Toray Industries, Inc.) with slits. Before fabrication, we cut the 0° plies at slit angle $+\theta$ and $-\theta$, and stacked these plies (Fig. 1a). The stacking configuration was $[0(+\theta)/90/0(-\theta \text{ or } +\theta)/90]_s$, with the slit angles indicated in parentheses.

Figure 1b presents the dimensions of the specimen. The specimen coupon was 210 mm long and 20 mm wide; three slits were introduced into all the 0° plies. GFRP tabs were glued at the ends of the specimen. Quasi-static tensile tests were carried out for these specimens with slits. We used a video microscope to observe the specimen surface near the slits during the tests. The specimens subjected to predetermined loading were then observed by a stereomicroscope and soft X-ray radiography.

We prepared the slit geometries listed in Table 1. A 0° ply with a slit angle of $+\theta$ and one with a $-\theta$ slit were alternately laminated in types IA, IB, and III. Slit width W_c was different between types IA and IB, and the height of the slit (H_c) was changed with the slit angle θ in these specimens. Type II had an identical slit angle $+\theta$ in all the 0° plies; the other geometries were the same as those of type IA. Type III had a constant slit height, and the width was then changed with the slit angle θ.

3. Experiment results

3.1 Tensile strength

Figure 2a plots tensile strengths as a function of the slit angle θ. Strength was almost independent of the angle θ in type IA, IB, and II specimens with a constant slit width, although misalignment of slits induced large variation. The strength of type IB was less than that of types IA and II. The strength of type III specimens, where the slit width was changed with the slit angle θ, decreased with increasing slit angle. Average strength was then plotted against the slit width W_c normalized by the specimen width W (Fig. 2b). Tensile strength linearly decreased with increasing slit width (or decreasing intact width). These results suggested that strength was independent of the inclined angle of slits.

The notch sensitivity would be changed with the slit width for specimens with a finite width. However, the damage extension with splits in the 0° plies, which will be described in the next section, could alleviate the stress concentration at the slit tips [15]. Accordingly, the change in the stress field near the slit tips with the slit angle would not be a dominant cause of final failure.

3.2 Damage process

Figure 3 presents soft X-ray photos of the type IA specimens with a slit angle of 90°. The damage process was almost the same as that by a penetrating notch. First, the slit was cracked at light loading, since the slit was closed and bonded only by the resin. Transverse cracks were then generated in the 90° plies just under the slit, due to the stress concentration of the cracked slit. These slits and transverse cracks were connected through the thickness, and the geometry became the same as that of a notch. Accordingly, we observed splits in the 0° plies from the slit tips along the fiber direction, transverse cracks in the 90° plies within the ligament area, and delamination from the slit tips along the splits.

Figure 4 depicts the observed damage progress in the type IA specimens with a slit angle of 45°. We found the following damage accumulation in these specimens. 1: The slit in the surface ply was cracked (Fig. 4a right). 2: The slits of inner plies were also cracked, and a transverse crack was generated at the crossing point of the slits (Fig. 4a left). 3: The slits were completely cracked, and the splits were initiated at the tips of slits. Transverse cracks in 90° plies accumulated under the slits. Moreover, the triangular region bounded by the slits and splits was completely delaminated (Fig. 4a center). 4: The splits in 0° plies extended, and the number of transverse cracks in the ligament area increased (Fig. 4b). We observed more transverse cracks near the slits. 5: Delamination extended in the ligament area along the splits (Fig. 4c).

The damage processes 1-3 were induced by the slits. Various types of damage could easily accumulate near the slits because of their low strength. After the slits were cracked in 0° plies, initial damage (e.g., the transverse crack in 90° plies and the delamination) was generated at the crossing point of the slits. The subsequent damage processes (4 and 5) were similar to those of notched laminates [9,16]. All the plies lost almost all load-bearing capacity near the slits because of the cracked slits and transverse cracks, as will be discussed later. Accordingly, the damage within the ligament area was similar to that of notched laminates, and the stress concentration at the tips of slits was reduced.

Figure 5 illustrates the fracture patterns of the type IA specimens with some slit angles. In situ observation verified that no fiber breakage occurred in the 0° ply before the final failure, and that all the specimens exhibited brittle fracture. The ligament area in the top 0° ply split into many pieces after progressive fiber breakages in the specimen with $\theta = 15°$. The specimen with $\theta = 45°$ was fractured by fiber breakages along the center line of the slits, not at the slit tips, after damage extended near the slits. Similar patterns were observed in the specimens with $\theta = 30°$, 60°, and 90°. These patterns for greater slit angles suggested that the position of the fracture was governed by the highest stress concentration generated along the central line of slits.

4. Analysis

4.1 Finite-element model

This study predicted the damage progress in cross-ply laminates with slits, by using a layer-wise finite-element model with cohesive elements proposed by the authors [16]. Figure 6 depicts the finite-element model for the type IA specimen with a slit angle of 45°, considering the symmetry for the through-thickness direction. The dimensions were 27.5 mm in the longitudinal (*x*) direction and 20 mm in the transverse (*y*) direction. The model was separated into four layers (two 0° layers and two 90° layers) to express the stacking configuration of $[(0/90)_2]_S$. Both layers were 0.125 mm thick, and four-node Mindlin plate elements were applied to these layers to address out-of-plane deformation. Table 2 lists the material properties used in this analysis; linear elastic behavior is assumed for all the plate elements.

Crack extension in the laminates was expressed using cohesive elements. Four-node cohesive elements were embedded in the two 0° layers along the $+\theta$ or $-\theta$ direction to represent the slits (Fig. 6b). Cohesive elements for splits were then located from the tips of the slits along the longitudinal (*x*) direction. We introduced only the three transverse cracks at the crossing point and tips of the slits (Fig. 6c), which could have a large effect on the damage progress, in order to reduce computation costs. Finally, eight-node cohesive elements for delamination were inserted into all the layer interfaces.

We used the cohesive element proposed by Geubelle et al. [17]; this element exhibited a bi-linear relation between the traction and the relative displacement of plate elements, and easily calculated mixed-mode cracking. The relation between the traction T and the relative displacement Δ was defined by using the parameter s as

$$T_i = \frac{s}{1-s}\frac{\Delta_i}{\Delta_{i\mathrm{c}}}\tau_{i\,\mathrm{max}} \qquad (i = \mathrm{n,\ t,\ b}), \tag{1}$$

$$\Delta_{\mathrm{nc}} = \frac{2G_{\mathrm{Ic}}}{\tau_{\mathrm{n\,max}}s_{\mathrm{ini}}},\ \Delta_{\mathrm{tc}} = \frac{2G_{\mathrm{IIc}}}{\tau_{\mathrm{t\,max}}s_{\mathrm{ini}}},\ \Delta_{\mathrm{bc}} = \frac{2G_{\mathrm{IIIc}}}{\tau_{\mathrm{b\,max}}s_{\mathrm{ini}}}, \tag{2}$$

where $\tau_{i\,\mathrm{max}}$ is the maximum stress and $\Delta_{i\mathrm{c}}$ (i = n, t, b) is the critical relative displacement; the subscripts n, t, and b indicate the cracking modes of normal tension, in-plane shear, and out-of-plane shear. The critical relative displacement when the element completely lost traction, Eq. (2), was defined by the energy criterion: $G_{i\mathrm{c}}$ (i = I, II, III) is the critical energy release rate, and s_{ini} is the initial value of the parameter s.

The parameter s, which defines the stiffness of the cohesive element, was calculated as a function of the normalized relative displacements $\tilde{\Delta} = \{\Delta_{\mathrm{n}}/\Delta_{\mathrm{nc}},\ \ \Delta_{\mathrm{t}}/\Delta_{\mathrm{tc}},\ \ \Delta_{\mathrm{b}}/\Delta_{\mathrm{bc}}\}^{T}$.

$$s = \min\left(s_{\min},\, \max\left(0, 1 - \left|\tilde{\Delta}\right|\right)\right). \tag{3}$$

This element acted as a penalty element during small relative displacement (i.e., $s = s_{\mathrm{ini}}$). The value of s became small with increasing relative displacement, and a cohesive element generated a crack surface that yielded no traction if $s = 0$. In the case of normal compressive relative displacement, $\Delta_{\mathrm{n}} < 0$, the decreasing process of the parameter s by Eq. (3) was neglected, and the cohesive element was assumed as a penalty element by temporarily setting $s = s_{\mathrm{ini}}$. Equation (3) indicated that the three cracking modes were coupled through the parameter s, and that the parameter represented the residual strength of the element. This calculation was nonlinear, since the stiffness of cohesive elements changed with the displacement field. Table 3 lists the properties of cohesive elements. It should be noted that these parameters were arranged from our experiments and literatures [18-21] and were not fitted to the experiment.

This study also predicted fiber breakages by the maximum stress criterion for longitudinal tension. This criterion avoided interference with the crack extension in cohesive elements that occurs using a criterion with shear terms. Stochastic strength distribution of reinforcing fibers was neglected, since the fracture pattern could be governed by the stress concentration due to the slits. When the stress field satisfied the criterion $\sigma_x = F_{\mathrm{L}}$ (= 2700 MPa; longitudinal tensile strength) in an element of 0° layers, we drastically reduced the stiffness of the element.

It seemed reasonable that the smaller longitudinal strength, e.g. the double of the strength for the specimen with the 0° slit (Type III), was used, if the strength of a specimen with slits was controlled by the width of the uncut ligaments. However, F_L based on this concept was much smaller than the strength of a unidirectional laminate, since the fibers of the 0° plies could be damaged by introducing the slits and the strength was reduced from the intrinsic strength of the 0° ply. Moreover, the smaller F_L could not represent the measured strengths in the simulation because of early fracture of the 0° layers. Based on the above consideration, the measured strength of a unidirectional laminate (2700 MPa) was applied to F_L in this simulation.

4.2 Simulation procedure

We evaluated the fiber breakages separately from the crack extension in cohesive elements. Figure 7 presents a flowchart of the simulation. The residual strength parameter s in all the cohesive elements was set at initial value s_{ini} (= 0.999 in this study) as the intact condition. The tensile displacement was applied to the model, and the displacement field was converged to predict the damage pattern in the laminate. Here, only the cohesive elements were evaluated as the nonlinear terms, and the residual strength parameter s was updated. After convergence of the displacement field considering cohesive elements, the maximum stress criterion was applied to all the plate elements in 0° layers to predict fiber breakages. If the longitudinal stress at an element exceeded the given strength, the longitudinal stiffness was reduced to a fraction of a thousand. This stiffness reduction process was performed element by element, for the element with the highest longitudinal stress. The crack extension in cohesive elements was then re-evaluated in the same loading condition. These procedures were iterated until no new fiber breakage was found. We analyzed the damage extension up to a given applied strain by increasing tensile displacement.

This simulation used the residual strength parameter s_{f} converged at the nth step as the initial value when evaluating the damage at the (n+1)th step. Here, the condition $s \leq s_{\mathrm{f}}$ was imposed on Eq. (3) to prevent the healing of the cracking process. This calculation used the direct iteration method [22] for convergence. This damage analysis was confirmed in our previous paper [16].

5. Simulated results and discussion

The edge along the x-direction was loaded by a uniform tensile displacement. The thermal residual stresses due to the temperature change in the curing process, ΔT = -100 K, were also considered. The slit geometry of θ = 90° was not analyzed, since the result would be the same as that of a laminate with a penetrating notch.

Figure 8 depicts the predicted typical damage patterns near slits (type IA laminate with $\theta = 45°$), where the completely broken cohesive elements in all the layers and interfaces were plotted. First, the cracks along the slits and the transverse crack were generated from the crossing point of slits (Fig. 8a). Delamination also extended from the crossing point of these cracks with extending ply cracks (Fig. 8b). When the cohesive elements of the slits were completely broken, the slit crack induced splitting in the 0° layers, and the triangular region bounded by the slits and splits was completely delaminated (Fig. 8c). These predicted damage patterns agreed well with the damage near the three slits observed in Fig. 4a. Figure 9 illustrates the calculated delamination at each layer interface, along with the ply cracks in the neighboring layers. We found that the delamination grew within the area between the slit and the transverse crack in the neighboring plies. The triangular region bounded by the slit, the split and the transverse crack then completely delaminated in all the ply interfaces, when the neighboring slit was entirely cracked. These results indicated that the delamination was induced by the preceding matrix cracking. Although splits and transverse cracks grew longer with increasing loading, only slight delamination appeared in the ligament area after the slit region was delaminated (Figs. 8d and 8e). This result coincided with the observation in Fig. 4, which indicated delamination progress in the ligament area just before the final failure. Many fibers broke in the third layer at 1.50% applied strain in this calculation.

Figure 10 depicts the distribution of in-plane shear stress in the surface 0° layer, along with the deformation. High shear stress was generated at the tips of a partly cracked slit (Fig. 10a). Splits were initiated at the slit tips after the slit was completely cracked, and the slit-split corners then exhibited large out-of-plane deformation. This result indicated that a completely delaminated slit region was caused by the interlaminar shear stress due to the difference of the in-plane shear deformation in the neighboring two plies, in addition to the out-of-plane deformation. Splits hardly extended to the other slit-split corner because of the low shear stress. Greater extension of splits was also predicted in the surface layer because of less restriction of the neighboring layer.

The tips of the slits generated only low shear stress in the ligament area, since it did not penetrate the laminate. Accordingly, the delamination did not extend in this region, unlike the damage in a laminate with a penetrating notch.

Figure 11 illustrates the distribution of the longitudinal stress in the inner 0° layer just before the final failure for a slit angle of 45°. The subsequent fiber breakages are plotted with the symbol x. The stress concentration was generated at the central line of the slits, not at the slit tips. The fiber breakages were then induced mostly near the central line of the slits by this stress concentration; this prediction coincided with the fracture patterns presented in Fig. 5. Although the distribution of fiber breakages was not symmetric contrary to the symmetric distribution of the longitudinal stress because of the calculation procedure, fiber breakages occurred in the opposite side of the slit with increasing applied strain. The distribution of fiber breakages for $\theta = 60°$ was similar to Fig. 11. However, in the case of 15° and 30° slits, the delamination extended to the model edges before fiber breakages were predicted. The large delamination in the ligament area could correspond to the fracture pattern with the exposed inner 90° ply for the 15° slit specimen (Fig. 5a).

In order to clarify the load-bearing capacity of the slit region, we calculated the stress fields for the following two virtual damage patterns in the laminate with 45° slit: (a) delamination in the slit region, which extended beyond the central line of slits, with a completely cracked slit region; and (b) the slit region with stiffness reduced to a fraction of a hundred of the original one to simulate the slit without load-bearing capacity. Figure 12 depicts the corresponding distribution of the longitudinal stress in the inner 0° layer. We found that both cases exhibited stress distribution similar to that depicted in Fig. 11, and that the large stress concentration appeared from the central line of slits to the delamination edge. These results suggested that significant stress concentration was generated by losing load-bearing capacity within the damaged slit region and by stacking these damaged slits at the same position. Consequently, the overall stress field near the slits became similar to that of a penetrating notch, when all the layers and interfaces were completely broken in the slit region. Furthermore, the size of the stress-concentrated region was small compared with the ligament width. The tensile strength could then be dependent on the width of the ligament area, as depicted in Fig. 2.

Figure 13 illustrates the simulated stress-strain curves of type IA laminates with some slit angles. We observed sharp drops in stress in all the slit angles. These drops were induced by sudden extension of delamination within the slit region after the slits were completely cracked. As indicated in Fig. 12, the overall slit region, rather than the slit tips, became the source of stress concentration, and the tensile strength then had little dependency on the slit angle. The predicted strengths were almost independent of slit angles; the strengths were about 550 MPa and were within the error range of the experiments due to the misalignment of the slits. The results of the experiment and the simulation supported the prediction of the strength for the specimen with slits, which was approximately estimated by the width of the uncut ligaments based on the global load sharing even if the damage existed near the ligament.

6. Conclusions

This study experimentally and numerically investigated fracture behavior in CFRP cross-ply laminates with initially cut fibers (slits) that could be introduced into composite components by using chopped strands, bending prepreg sheets, or cutting preforms. To this end, we experimentally observed the damage near the slit in detail, and numerically evaluated the damage progress by damage analysis with cohesive elements and a damage law. The conclusions are summarized below.

1. The slit was easily cracked by light loading, and transverse cracks accumulated in the slit region. These cracks were generated from the crossing point of the slits. Furthermore, the triangular region bounded by the slit, the split, and the transverse crack in the neighboring layers simultaneously delaminated because of the interlaminar shear stress generated by the difference of the in-plane shear deformation in the neighboring layers.
2. The damage process in the ligament area was similar to that of a laminate with a penetrating notch, since the slit region lost almost all load-bearing capacity due to the accumulation of

damage.

3. The longitudinal stress was concentrated at the central line of slits, regardless of slit angle, and the fiber breakages were induced mostly near the highest stress concentration. The predicted tensile strength had little dependency on the slit angle, since the damage extension reduced the stress concentration near the slit tips, and since the overall slit region became the source of stress concentration.

Thus, this study qualitatively illustrated the fracture process in the cross-ply laminate with slits. However, some ply cracks in the slit region were neglected for simplicity, and the criterion for the fiber failure was primitive. Detailed model for these damage types will provide quantitative prediction of the fracture behavior.

References

[1] Marissen R, Linsen J. Variability of the flexural strength of sheet moulding compounds. Compos Sci Technol 1999; 59(14): 2093-2100.

[2] Van Voorn B, Smit HHG, Sinke RJ, de Klerk B. Natural fibre reinforced sheet moulding compound. Compos Part A 2001; 32(9): 1271-1279.

[3] Oldenbo M, Fernberg SP, Berglund LA. Mechanical behaviour of SMC composites with toughening and low density additives. Compos Part A 2003; 34(9): 875-885.

[4] Taketa I, Kitano A, Okabe T. A new compression molding approach with unidirectionally arrayed chopped strands (UACS). In: Proceedings of 32nd Symposium on Composite Materials. Nagasaki, October, 2007. p. 63-64 (In Japanese).

[5] Taketa I, Okabe T, Kitano A. A New compression-molding approach using unidirectionally arrayed chopped strands. Compos Part A; in press.

[6] Chang KY, Liu S, Chang FK. Damage tolerance of laminated composites containing an open hole and subjected to tensile loadings. J Compos Mater 1991; 25(3): 274-301.

[7] Choi SW, Song EJ, Hahn HT. Prediction of fatigue damage growth in notched composite

laminates using an artificial neural network. Compos Sci Technol 2003; 63(5): 661-675.

[8] Belmonte HMS, Ogin SL, Smith PA, Lewin R. A physically-based model for the notched strength of woven quasi-isotropic CFRP laminates. Compos Part A 2004; 35(7-8): 763-778.

[9] Kortschot MT, Beaumont PWR. Damage mechanics of composite materials: I. Measurements of damage and strength. Compos Sci Technol 1990; 39(4): 289-301.

[10] Kortschot MT, Beaumont PWR. Damage mechanics of composite materials. II. A damaged-based notched strength model. Compos Sci Technol 1990; 39(4): 303-326.

[11] Spearing SM, Beaumont PWR. Fatigue damage mechanics of composite materials. I: Experimental measurement of damage and post-fatigue properties. Compos Sci Technol 1992; 44(2): 159-168.

[12] Spearing SM, Beaumont PWR, Ashby MF. Fatigue damage mechanics of composite materials. II: A damage growth model, Compos Sci Technol 1992; 44(2): 169-177.

[13] Olsson R, Iwarsson J, Melin LG, Sjögren A, Sterk JC. Experiments and analysis of laminates with artificial damage. Compos Sci Technol 2003; 63(2): 199-209.

[14] Craven R, Sztefek P, Olsson R. Investigation of impact damage in multi-directional tape laminates and its effect on local tensile stiffness. Compos Sci Technol 2008; 68(12): 2518-2525.

[15] Awerbuch J, Madhukar MS. Notched strength of composite laminates: predictions and experiments – a review. J Reinf Plast Compos 1985; 4(1): 3-159.

[16] Yashiro S, Takeda N, Okabe T, Sekine H. A new approach to predicting multiple damage states in composite laminates with embedded FBG sensors. Compos Sci Technol 2005; 65(3-4): 659-67.

[17] Geubelle PH, Baylor JS. Impact-induced delamination of composites: a 2D simulation. Compos Part B 1998; 29(5): 589-602.

[18] Hojo M, Ochiai S, Gustafson CG, Tanaka K. Effect of matrix resin on delamination fatigue crack growth in CFRP laminates. Eng Fract Mech 1994; 49(1): 35-47.

[19] Hojo M, Matsuda S, Tanaka M, Ochiai S, Murakami A. Mode I delamination fatigue

properties of interlayer-toughened CF/epoxy laminates. Compos Sci Technol 2006; 66(5): 665-675.

[20] Toray Industries. Fundamentals of carbon fiber technology and their application to Torayca products. http://www.torayca.com/techref/ (Accessed 24 February 2009).

[21] Japan Aerospace Exploration Agency (JAXA). Advanced Composites Database System: JAXA-ACDB. http://www.jaxa-acdb.com/ (Accessed 24 February 2009).

[22] Owen DRJ, Hinton E, Finite Elements in Plasticity. Swansea: Pineridge Press, 1980.

Figure captions

Fig. 1 CFRP cross-ply laminate with slits.

Fig. 2 Effect of slit geometries on tensile strength of the laminate with slits.

Fig. 3 X-ray photos of the specimens with a slit angle of 90°. The tensile strength σ_b was 494 MPa. Transverse cracks did not appear in the photos because of low resolution.

Fig. 4 X-ray photos of the specimens with a slit angle of 45°. The tensile strength σ_b was 538 MPa.

Fig. 5 Fracture behavior in the specimens with slits (type IA).

Fig. 6 Layer-wise finite-element model with cohesive elements for the cross-ply laminate with slits (slit angle $\theta = 45°$).

Fig. 7 Flowchart of the simulation. Fiber breakages were evaluated separately from the crack extension in cohesive elements.

Fig. 8 Predicted damage patterns in the cross-ply laminate with slits, where σ_b (= 557 MPa) was the maximum stress at the final failure in the simulation.

Fig. 9 Damage extension in each layer interface.

Fig. 10 Distribution of the in-plane shear stress in the top 0° layer. Displacement in the through-thickness direction was magnified.

Fig. 11 Distribution of the longitudinal stress in the third 0° layer at the last step just before the final failure (1.49% strain) for a slit angle of 45°. The subsequent fiber breakage points were also plotted with the symbol x.

Fig. 12 Longitudinal stress distribution in the third 0° layer at 1.0% applied strain. The following damage patterns were assumed: (a) delaminated slit region with ply cracks, and (b) reduced stiffness within the slit region (without damage).

Fig. 13 Simulated stress-strain curves of type IA laminates for some slit angles.

Table captions

Table 1 Dimensions of the cut fibers.

Table 2 Material properties of the CFRP laminate.

Table 3 Properties of cohesive elements.

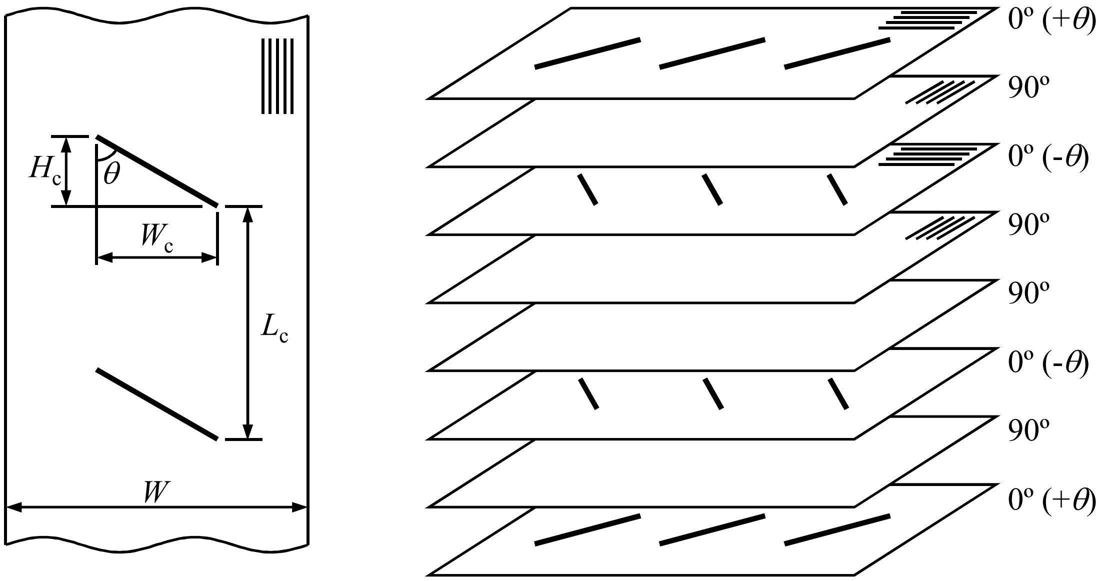

(a) Schematic of stacking

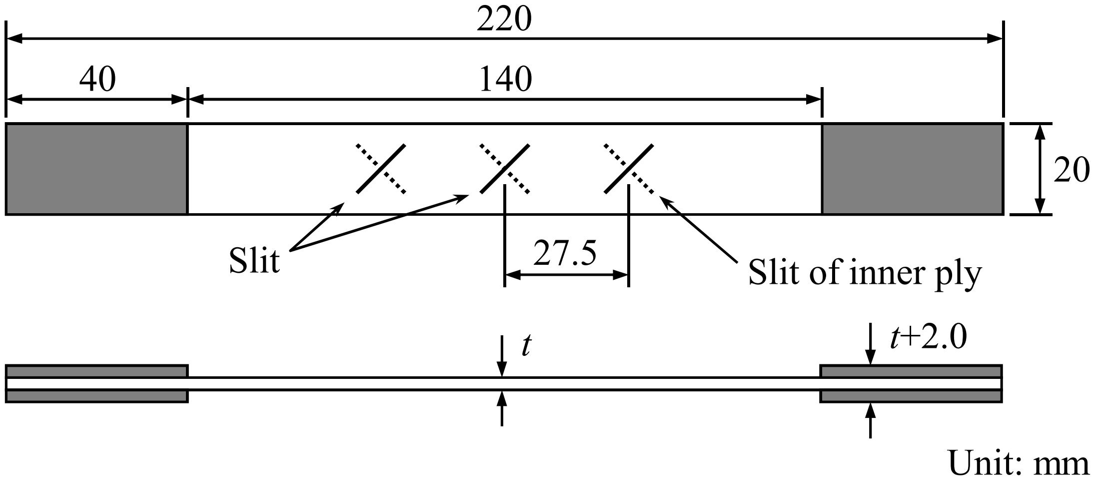

(b) Dimensions of the specimen

Fig. 1 CFRP cross-ply laminate with slits.

Fig. 2

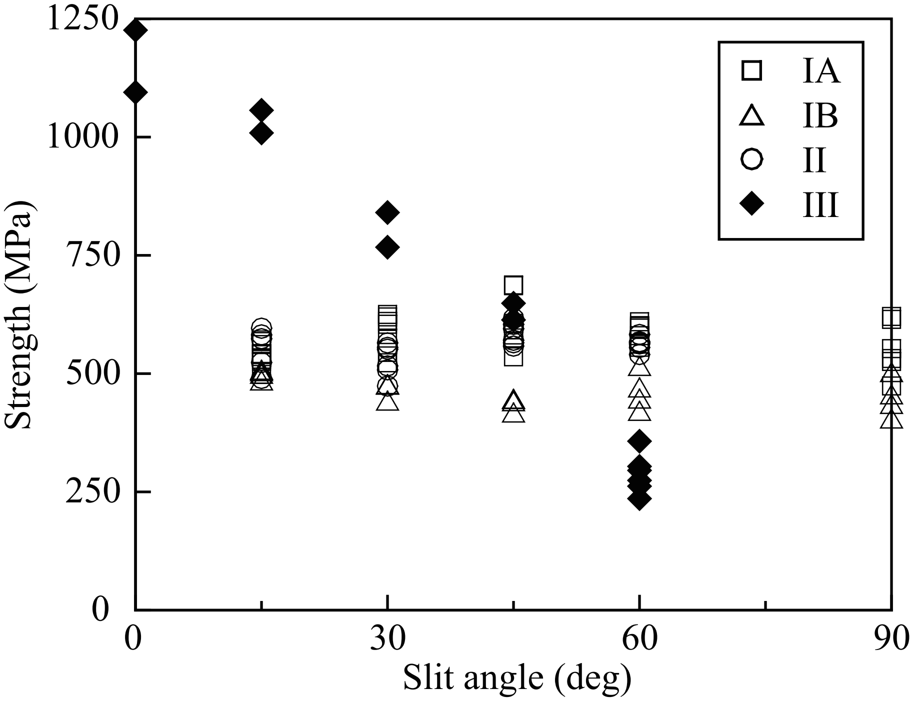

(a) Slit angle

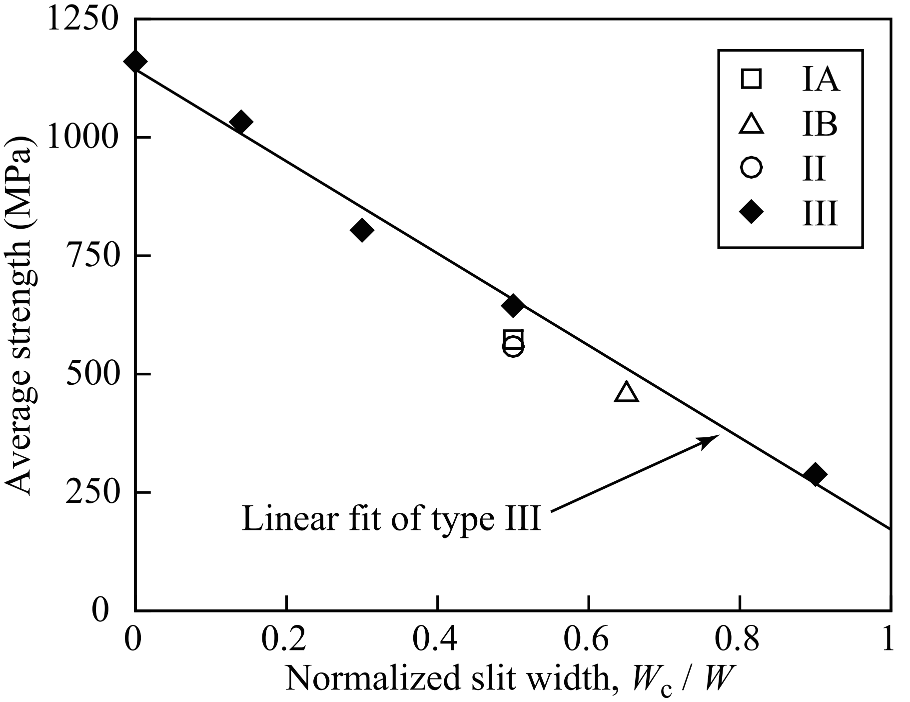

(b) Slit width

Fig. 2 Effect of slit geometries on tensile strength of the laminate with slits.

Fig. 3

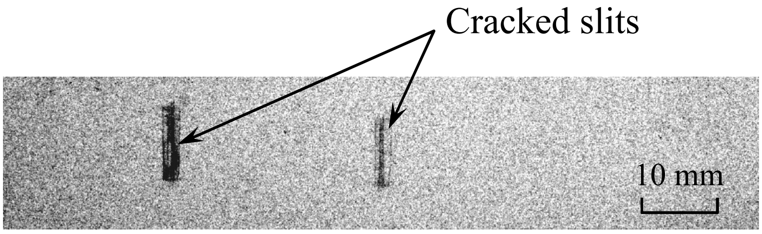

(a) $0.5\sigma_b$

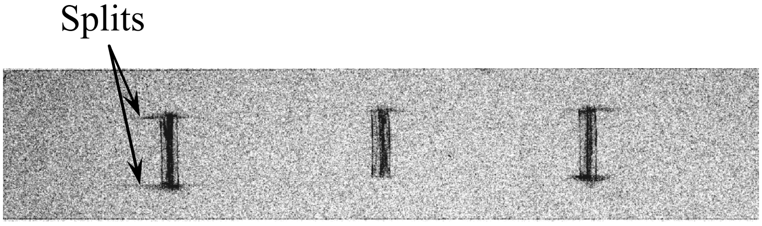

(b) $0.8\sigma_b$

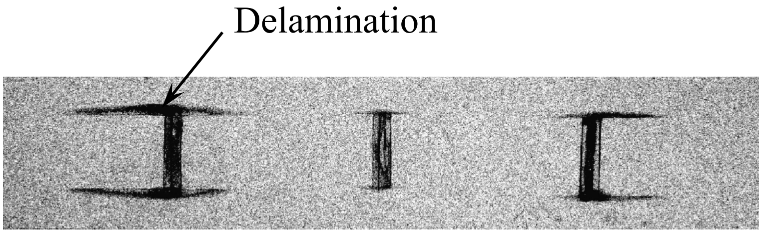

(c) $0.95\sigma_b$

Fig. 3 X-ray photos of the specimens with a slit angle of 90º. The tensile strength σ_b was 494 MPa. Transverse cracks did not appear in the photos because of low resolution.

Fig. 4

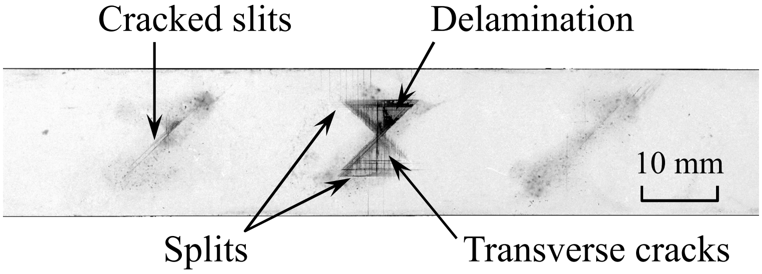

(a) $0.5\sigma_b$

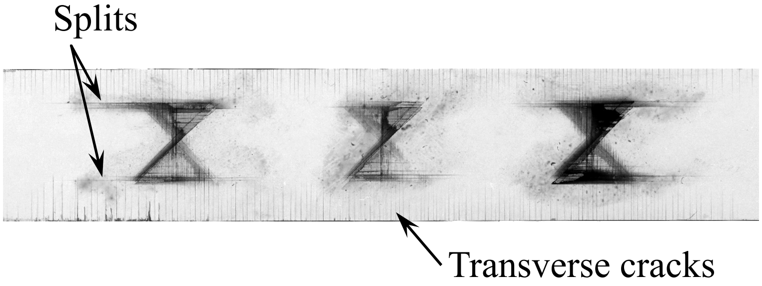

(b) $0.8\sigma_b$

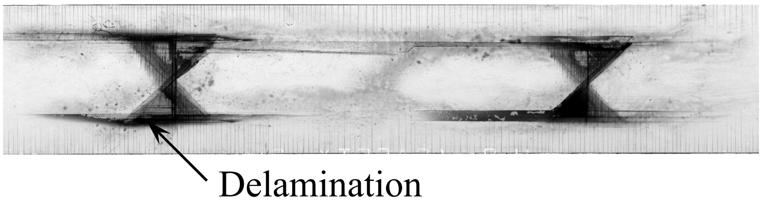

(c) $0.9\sigma_b$

Fig. 4 X-ray photos of the specimens with a slit angle of 45º. The tensile strength σ_b was 538 MPa.

Fig. 5

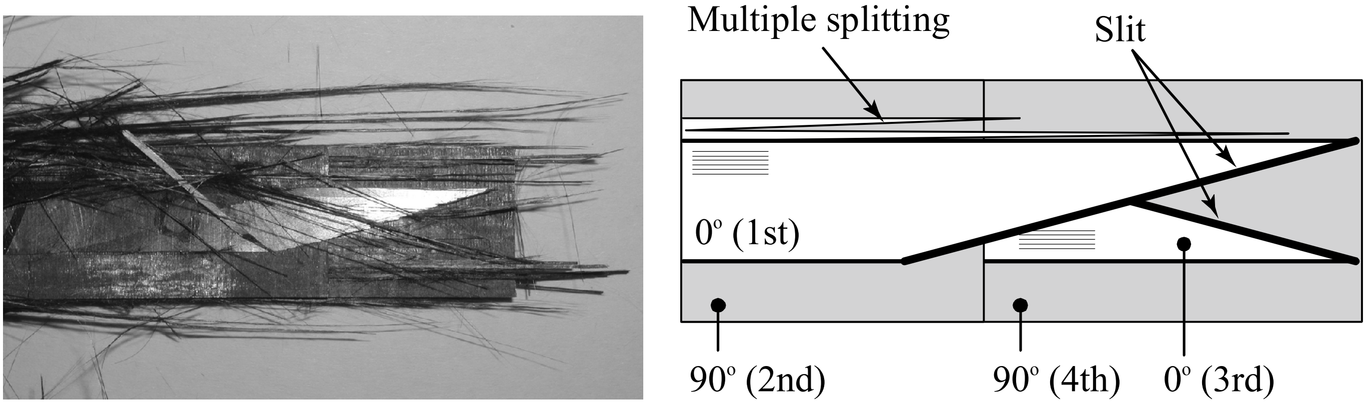

(a) $\theta = 15^\circ$

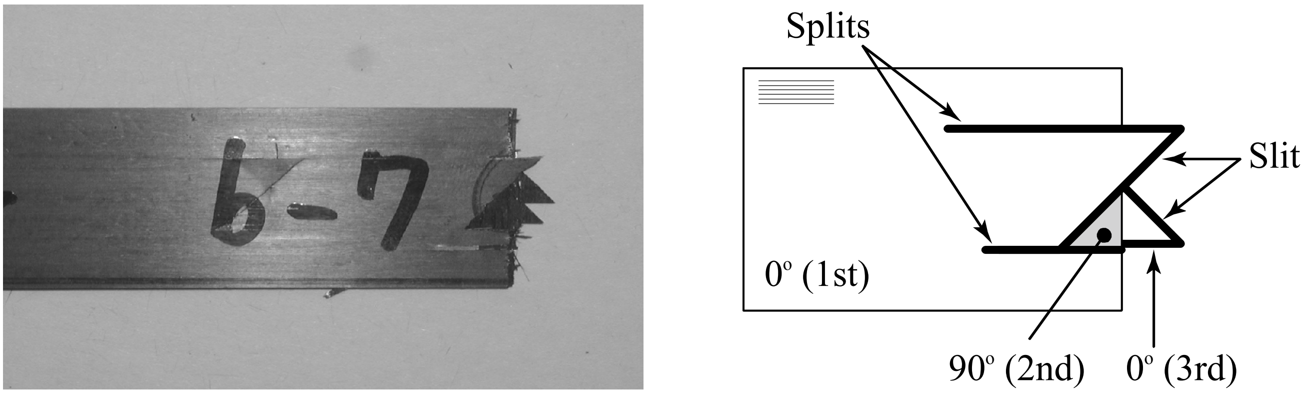

(b) $\theta = 45^\circ$

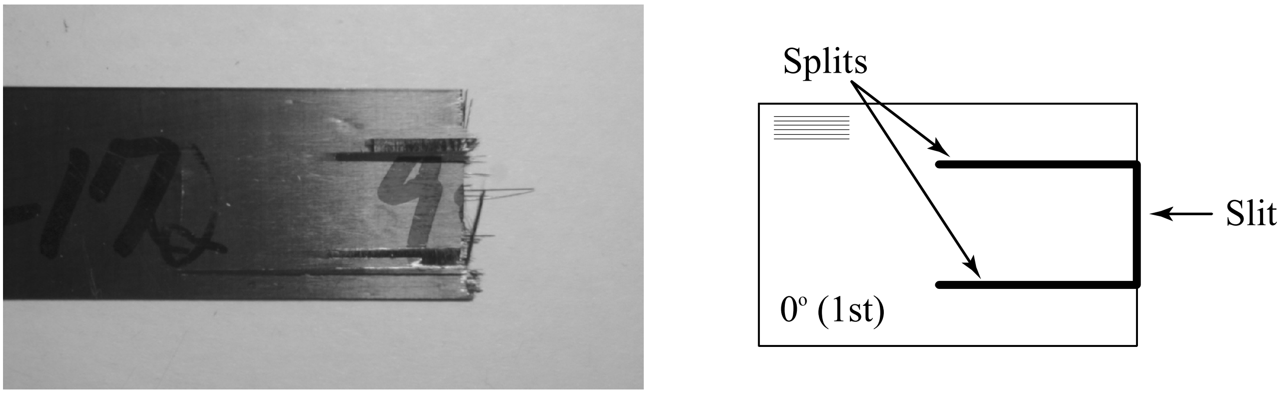

(c) $\theta = 90^\circ$

Fig. 5 Fracture behavior in the specimens with slits (type IA).

Fig. 6

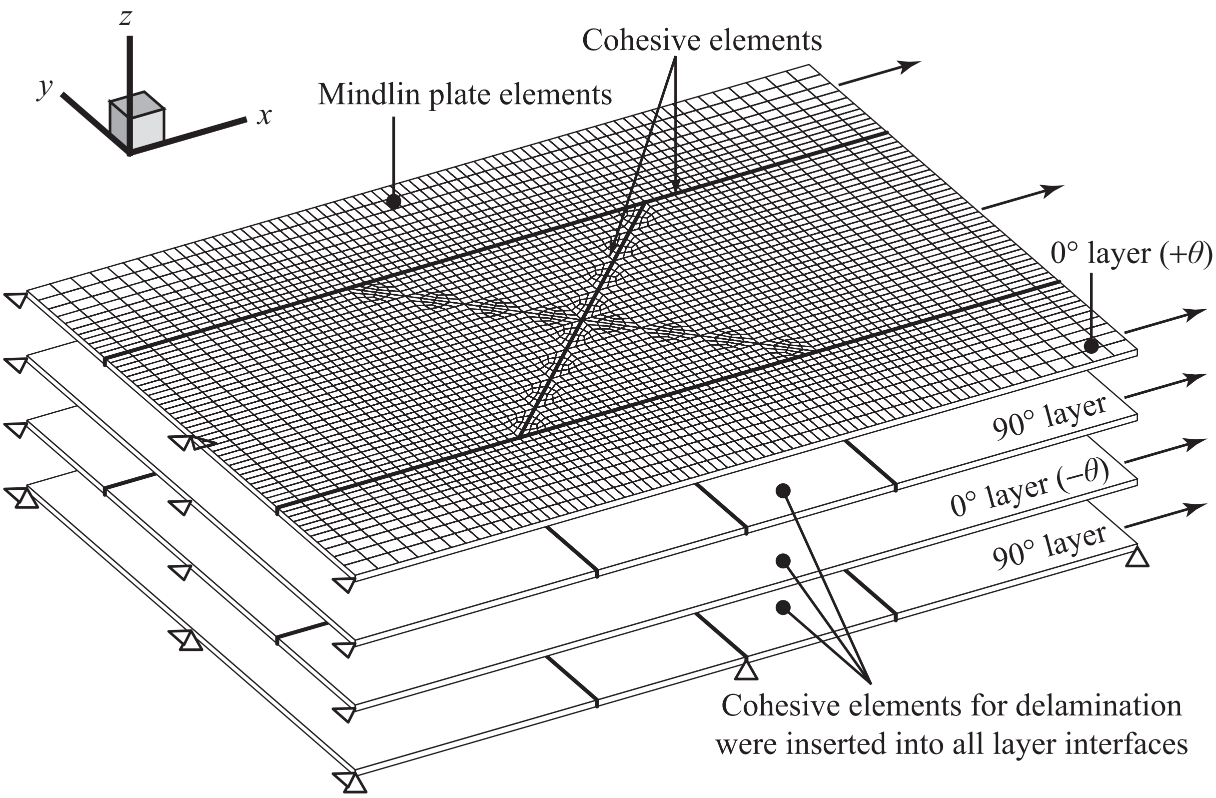

(a) Overview

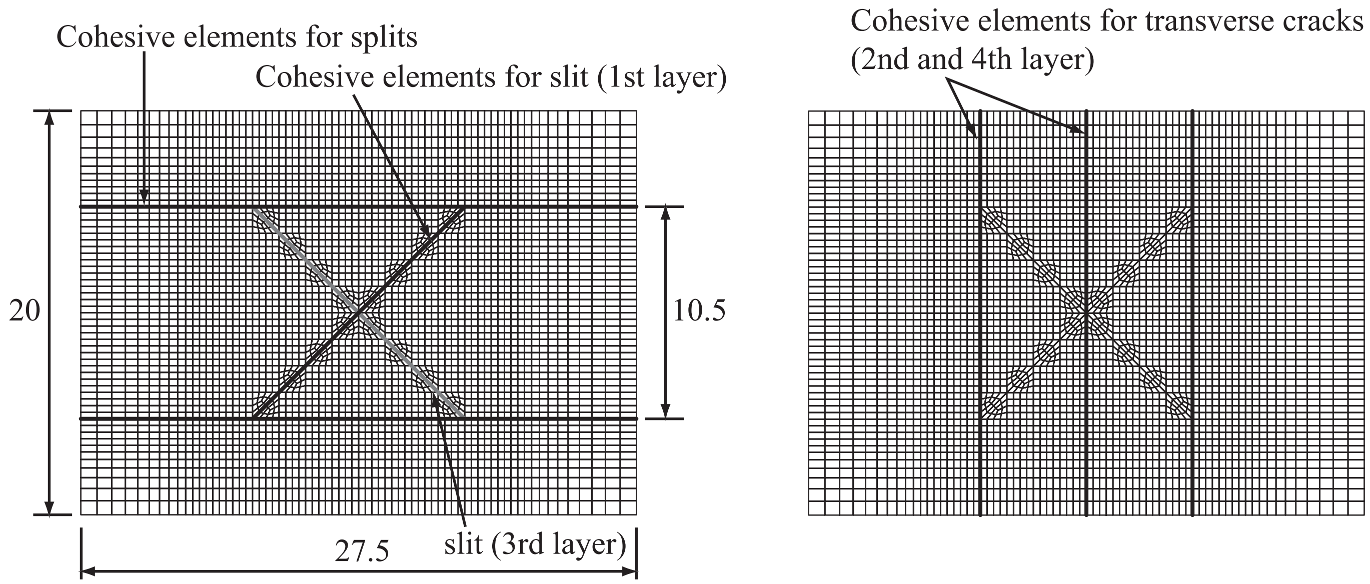

(b) 0° layer

(c) 90° layer

Fig. 6 Layer-wise finite-element model with cohesive elements for the cross-ply laminate with slits (slit angle $\theta = 45°$).

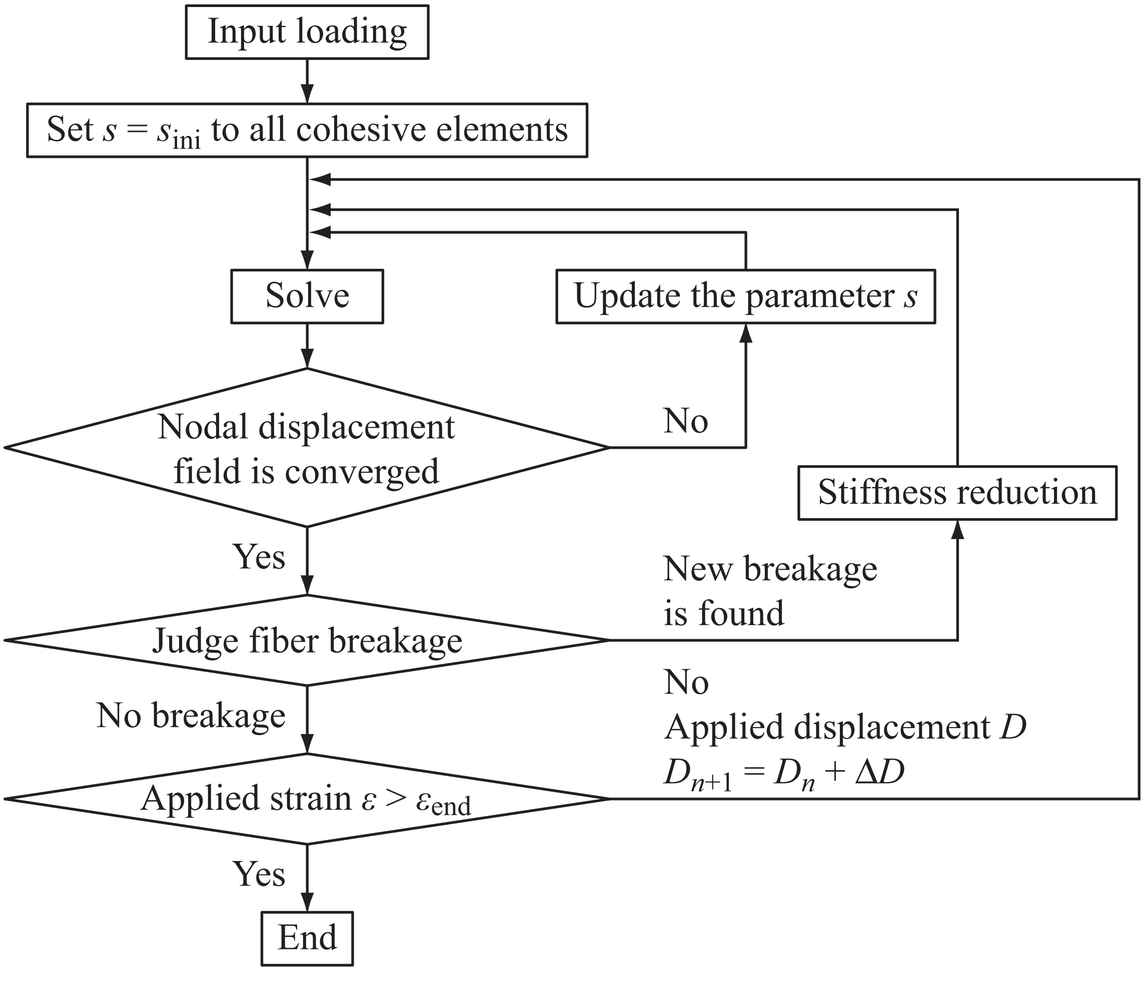

Fig. 7 Flowchart of the simulation. Fiber breakages were evaluated separately from the crack extension in cohesive elements.

Fig. 8

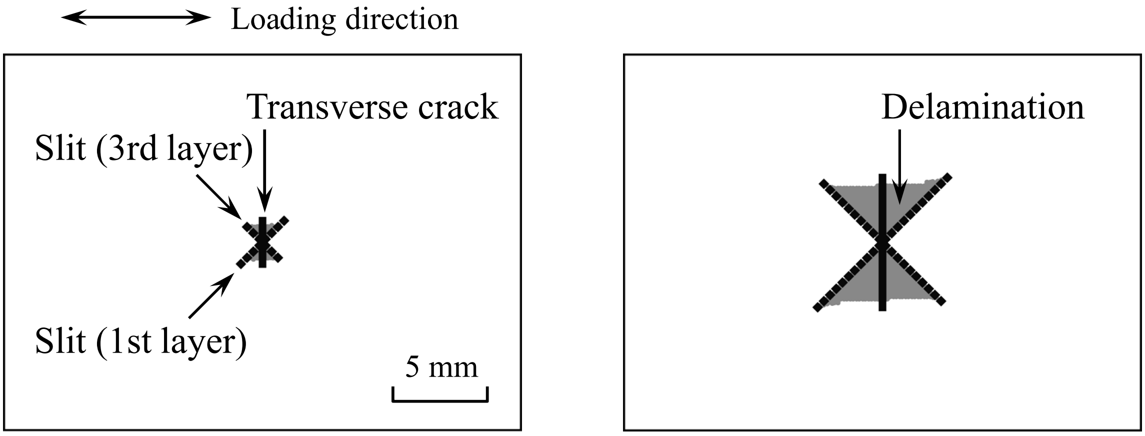

(a) 0.28% (0.34 σ_b)

(b) 0.35% (0.36 σ_b)

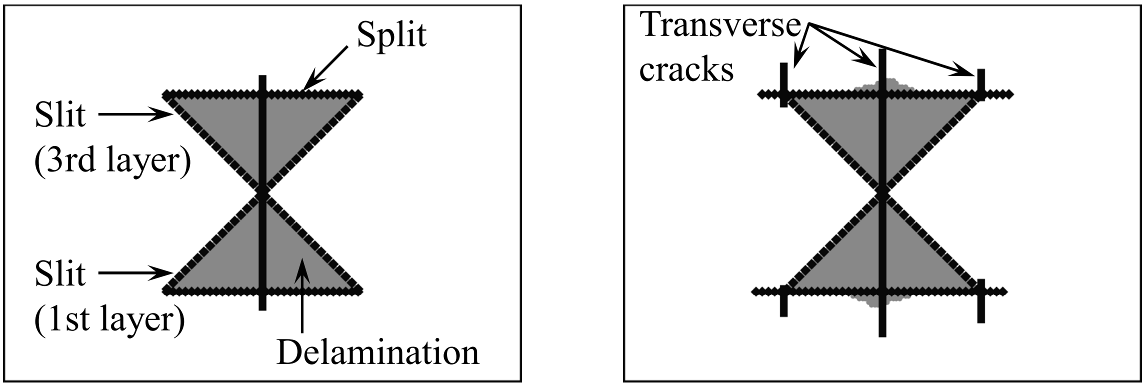

(c) 0.53% (0.38 σ_b)

(d) 0.86% (0.62 σ_b)

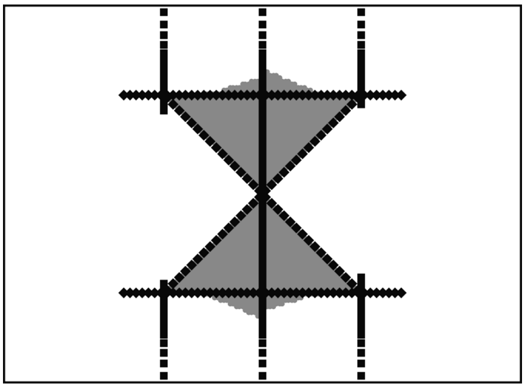

(e) 0.98% (0.7 σ_b)

Fig. 8 Predicted damage patterns in the cross-ply laminate with slits, where σ_b (= 557 MPa) was the maximum stress at the final failure in the simulation.

Fig. 9

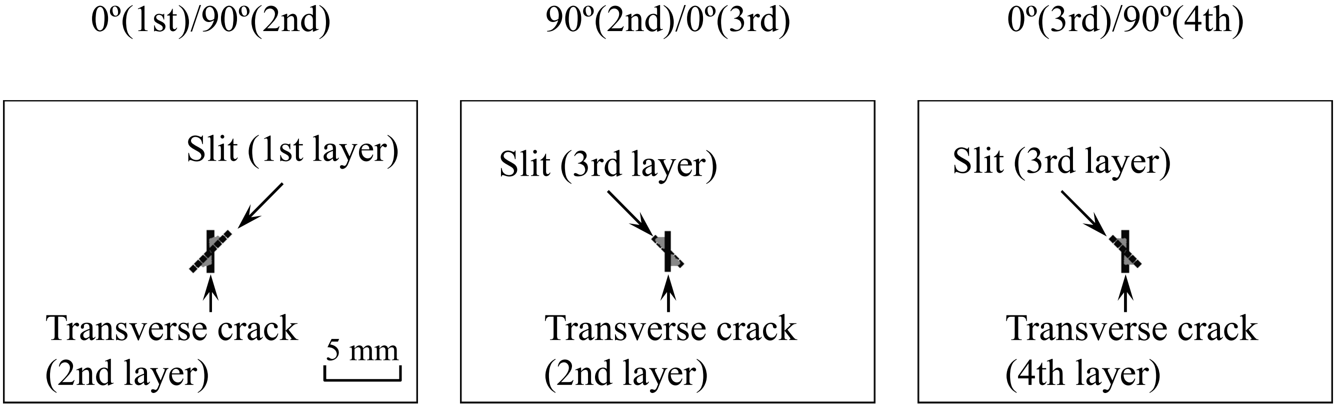

(a) 0.28% (0.34 σ_b)

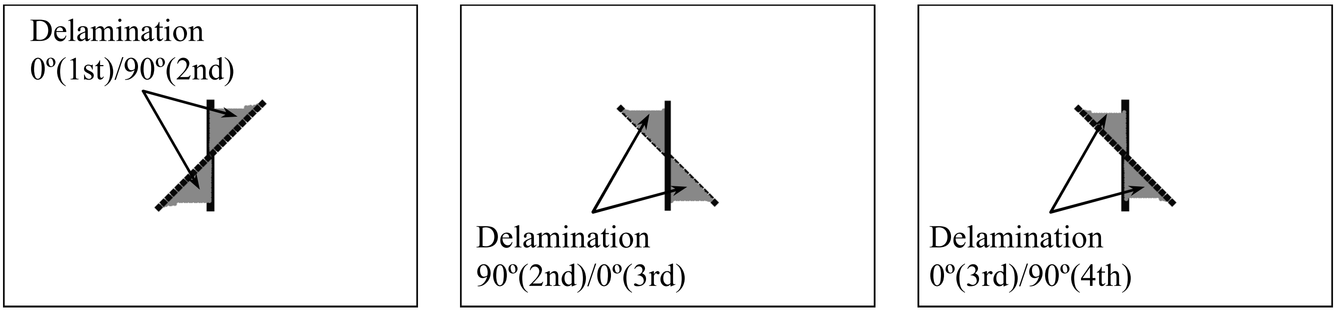

(b) 0.35% (0.36 σ_b)

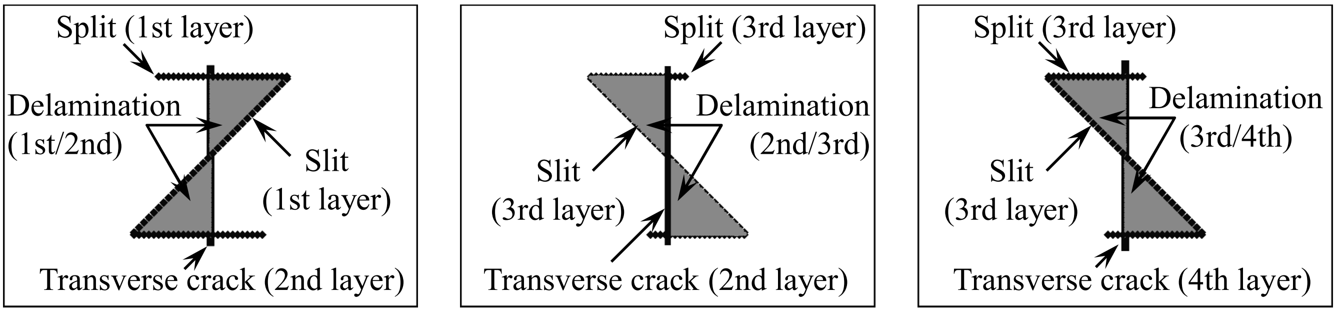

(c) 0.53% (0.38 σ_b)

Fig. 9 Damage extension in each layer interface.

Fig. 10

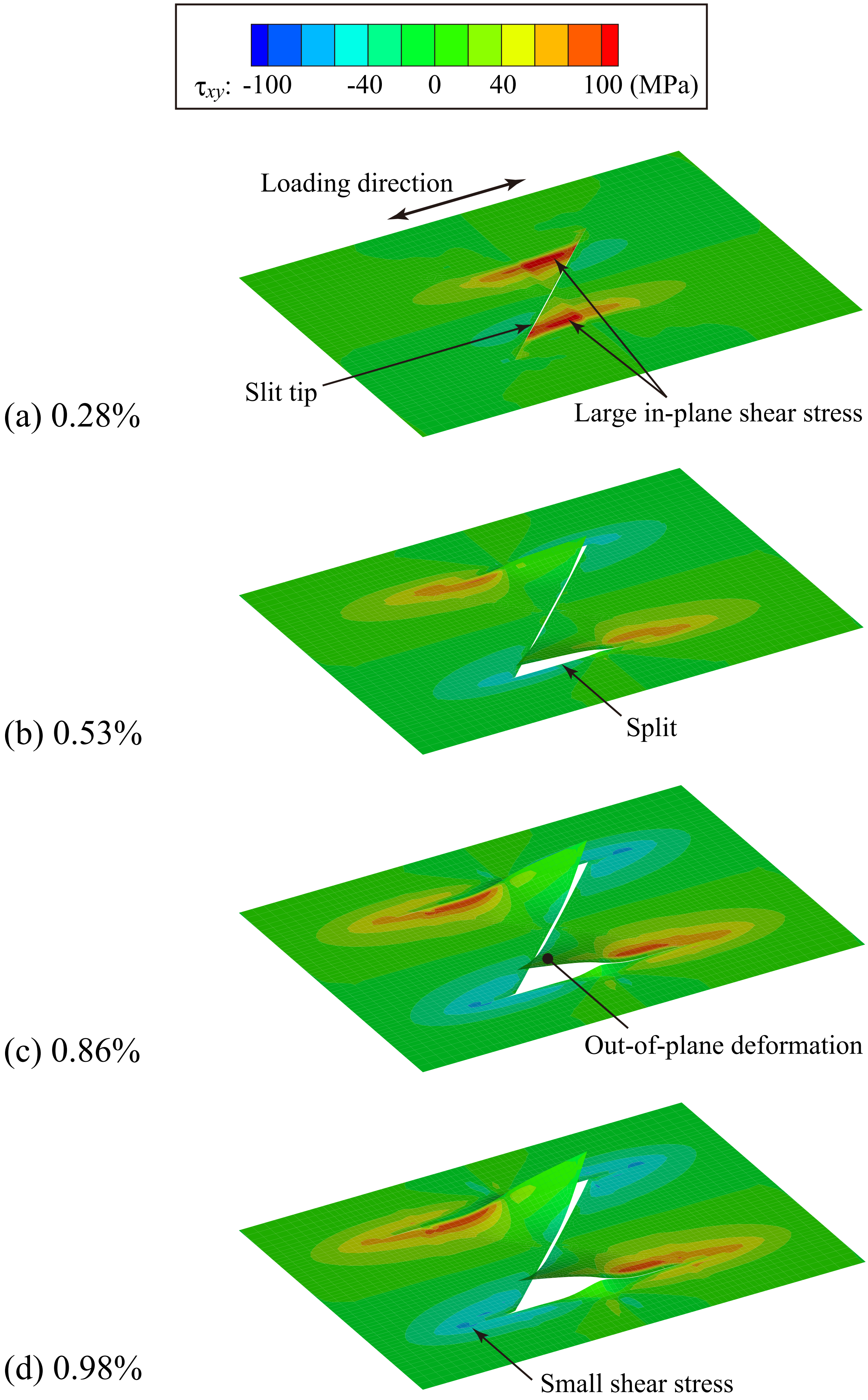

Fig. 10 Distribution of the in-plane shear stress in the top 0° layer. Displacement in the through-thickness direction was magnified.

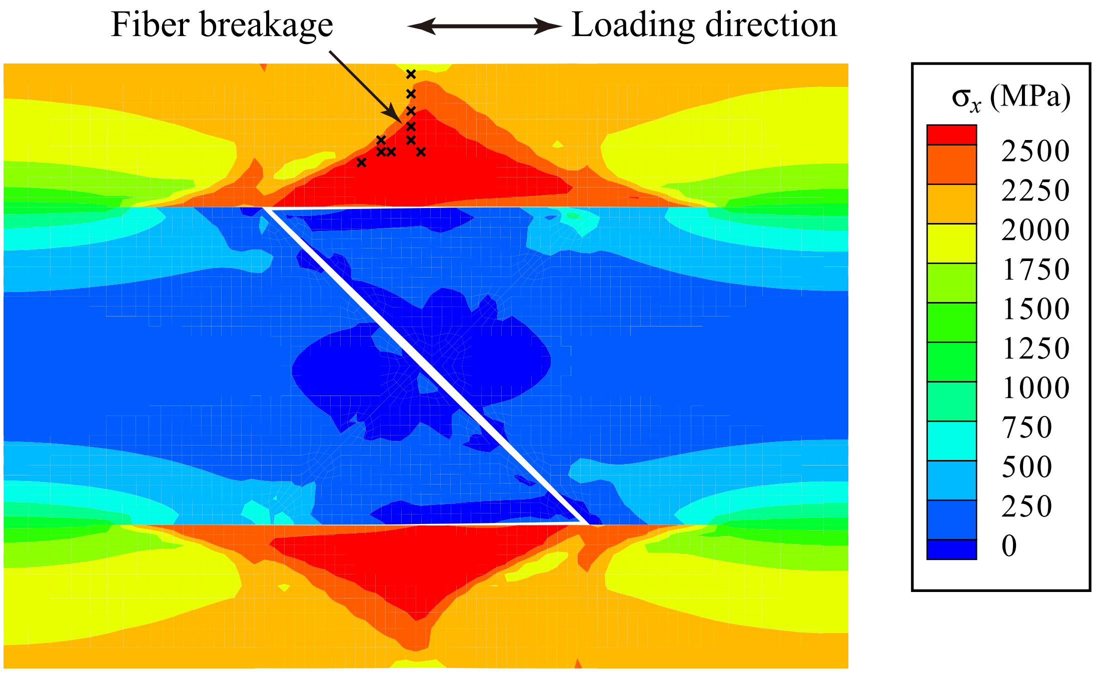

Fig. 11 Distribution of the longitudinal stress in the third 0° layer at the last step just before the final failure (1.49% strain) for a slit angle of 45°.

The subsequent fiber breakage points were also plotted with the symbol x.

Fig. 12

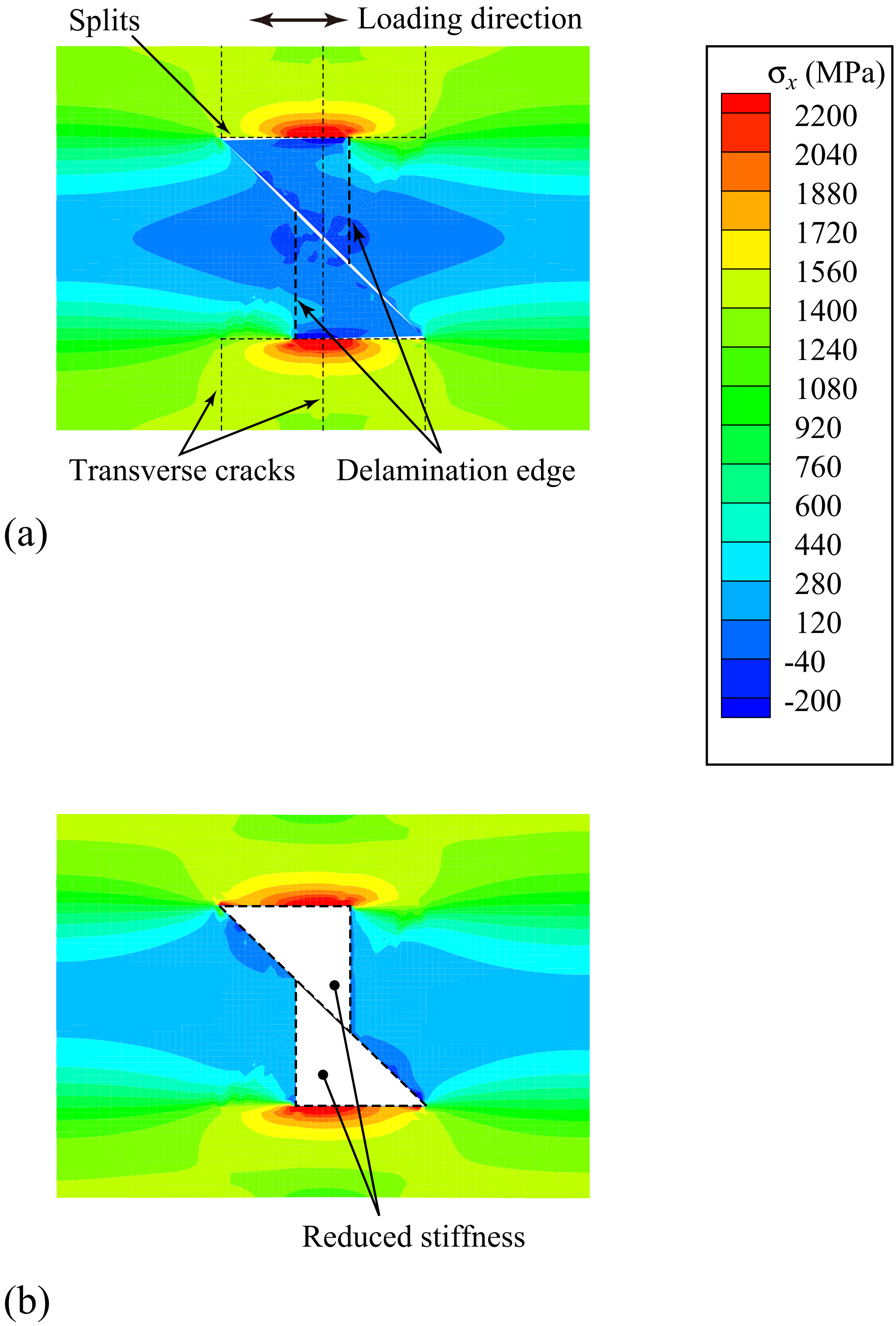

(a)

(b)

Fig. 12 Longitudinal stress distribution in the third 0° layer at 1.0% applied strain. The following damage patterns were assumed: (a) delaminated slit region with ply cracks, and (b) reduced stiffness within the slit region (without damage).

Fig. 13

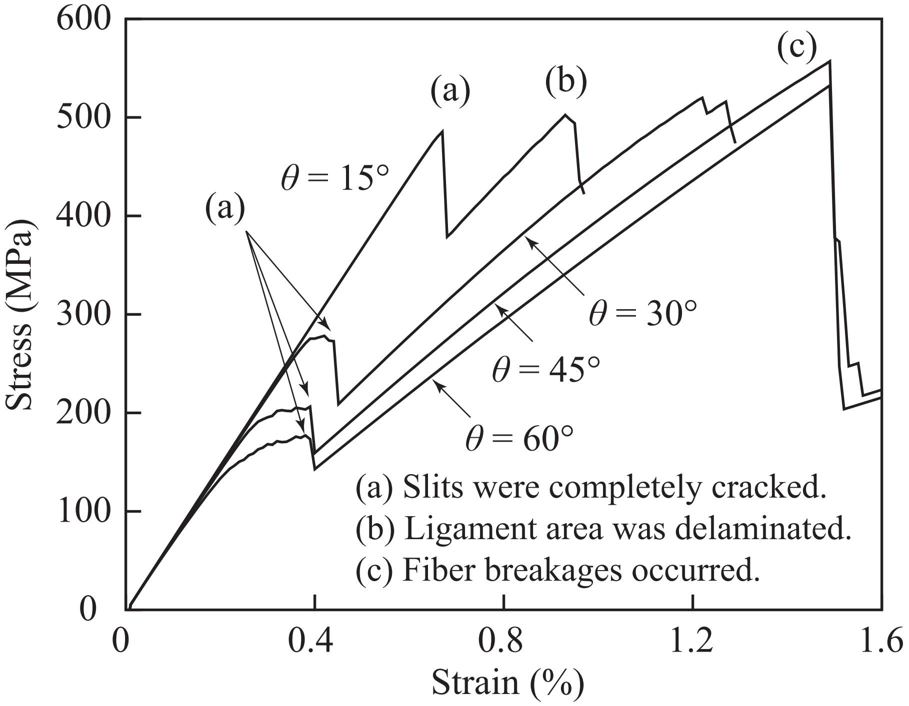

Fig. 13 Simulated stress-strain curves of type IA lamiantes for some slit angles.

Table 1 Dimensions of the cut fibers.

	IA	IB	II	III
W (mm)	20.0	20.0	20.0	20.0
W_c (mm)	10.5	13.0	10.5	$H_c \tan\theta$
H_c (mm)	$W_c/\tan\theta$	$W_c/\tan\theta$	$W_c/\tan\theta$	10.5
L_c (mm)	27.5	27.5	27.5	20.0
θ	15°, 30°, 45°, 60°, 90°			
Slit angle	$\pm\theta$	$\pm\theta$	$+\theta$	$\pm\theta$

Table 2 Material properties of the CFRP laminate.

Longitudinal Young's modulus (GPa)	135
Transverse Young's modulus (GPa)	8.2
In-plane shear modulus (GPa)	4.8
Out-of-plane shear modulus (GPa)	3.5
In-plane Poisson's ratio	0.31
Out-of-plane Poisson's ratio	0.49
Longitudinal thermal expansion coefficient ($\times 10^{-6}$/K)	0.3
Transverse thermal expansion coefficient ($\times 10^{-6}$/K)	36.5

Table 3 Properties of cohesive elements.

	Splits Transverse cracks	Slits Delamination
In-plane tensile strength (MPa)	76	30
In-plane shear strength (MPa)	100	60
Out-of-plane shear strength (MPa)	100	60
Mode I critical energy release rate (J/m^2)	150	200
Mode II critical energy release rate (J/m^2)	300	600
Mode III critical energy release rate (J/m^2)	300	600